

# A filament of dark matter between two clusters of galaxies

Jörg P. Dietrich<sup>1</sup>, Norbert Werner<sup>2</sup>, Douglas Clowe<sup>3</sup>, Alexis Finoguenov<sup>4</sup>, Tom Kitching<sup>5</sup>, Lance Miller<sup>6</sup> & Aurora Simionescu<sup>2</sup>

<sup>1</sup>*Physics Dept. and Michigan Center for Theoretical Physics, University of Michigan, 450 Church Street, Ann Arbor, MI 48109-1040, USA*

<sup>2</sup>*Kavli Institute for Particle Astrophysics and Cosmology, Stanford University, 382 Via Pueblo Mall, Stanford, CA 94305-4060, USA*

<sup>3</sup>*Dept. of Physics & Astronomy, Ohio University, Clippinger Lab 251B, Athens, OH 45701, USA*

<sup>4</sup>*Max-Planck-Institut für extraterrestrische Physik, Giessenbachstraße, 85748 Garching b. München, Germany*

<sup>5</sup>*Institute for Astronomy, The University of Edinburgh, Royal Observatory, Blackford Hill, Edinburgh EH9 3HJ, U.K.*

<sup>6</sup>*Department of Physics, University of Oxford, The Denys Wilkinson Building, Keble Road, Oxford OX1 3RH, U.K.*

**It is a firm prediction of the concordance Cold Dark Matter (CDM) cosmological model that galaxy clusters live at the intersection of large-scale structure filaments<sup>1</sup>. The thread-like structure of this “cosmic web” has been traced by galaxy redshift surveys for decades<sup>2,3</sup>. More recently the Warm-Hot Intergalactic Medium (WHIM) residing in low redshift filaments has been observed in emission<sup>4</sup> and absorption<sup>5,6</sup>. However, a reliable direct detection of the underlying Dark Matter skeleton, which should contain more than half of all matter<sup>7</sup>, remained elusive, as earlier candidates for such detections<sup>2,9,10</sup> were either falsified<sup>11,12</sup> or suffered from low signal-to-noise ratios<sup>8,10</sup> and unphysical misalignments of dark and luminous matter<sup>9,10</sup>. Here we report the detection of a dark matter filament connecting the two main components of the Abell 222/223 supercluster system from its weak gravitational lensing signal, both in a non-parametric mass reconstruction and in parametric model fits. This filament is coincident with an overdensity of galaxies<sup>10,13</sup> and diffuse, soft X-ray emission<sup>4</sup> and contributes mass comparable to that of an additional galaxy cluster to the total mass of the supercluster. Combined with X-ray observations<sup>4</sup>, we place an upper limit of 0.09 on the hot gas fraction, the mass of X-ray emitting gas divided by the total mass, in the filament.**

Abell 222 and Abell 223, the latter a double galaxy cluster in itself, form a supercluster system of three galaxy clusters at a redshift of  $z \sim 0.21$  [ref. 13], separated on the sky by  $\sim 14'$ . Gravitational lensing distorts the images of faint background galaxies as their light passes massive foreground structures. The foreground mass and its distribution can be deduced from measuring the shear field imprinted on the shapes of the background galaxies. Additional information on this process is given in the supplementary information. The mass reconstruction in Figure 1 shows a mass bridge connecting A 222 and the southern component of A 223 (A 223-S) at the  $4.1\sigma$  significance level. This mass reconstruction does not assume any model or physical prior on the mass distribution.

To show that the mass bridge extending between A 222 and A 223 is not caused by the overlap of the cluster halos but in fact due to additional mass, we also fit parametric models to the three clusters plus a filament component. The clusters were modelled as elliptical Navarro-Frenk-White (NFW) profiles<sup>14</sup> with a fixed mass-concentration relation<sup>15</sup>. We used a simple model for the filament, with a flat ridge line connecting the clusters, exponential cut-offs at the filament end points in the clusters, and a King profile<sup>16</sup> describing the radial density distribution, as suggested by previous studies<sup>17,18</sup>. We show in the supplementary information that the exact ellipticity has little impact on the significance of the filament.

The best fit parameters of this model were determined with a Monte-Carlo Markov Chain (MCMC) and are shown in Fig. 2. The likelihood-ratio test prefers models with a filament component with 96.0% confidence over a fit with three NFW halos only. A small degeneracy exists in the model between the strength of the filament and the virial radii of A 222 and A 223-S. The fitting procedure tries to keep the total amount of mass in the supercluster system constant at the level indicated by the observed reduced shear. Thus, it is not necessarily the case that sample points with a positive filament contribution indeed have more mass in the filament area than a 3 clusters only model has. The reason is that the additional filament mass might be compensated for with lower cluster masses. We find that the integrated surface mass density along the filament ridge line exceeds that of the clusters only model in 98.5% of all sample points. This indicates that the data strongly prefers models with additional mass between A 222 and A 223-S and that this preference is stronger than the confidence level derived from the likelihood-ratio test. The difference is probably due to the oversimplified model, which is not a good representation of the true filament shape. The data on the other hand is not able to constrain more complex models. Extensions to the simple model we tried were replacing the flat ridge line with a parabola as well as replacing the King profile with a cored profile leaving the exponent free. The latter was essentially unconstrained. The parabolic ridge line model produced a marginally better fit that, however, was statistically consistent with the flat model. Moreover, the likelihood-ratio test did not find a preference for the parabolic shape.

The virial masses inferred from the MCMC are lower than those reported earlier for this system<sup>10</sup>, which were obtained from fitting a circular two-component NFW model to A 222 and A 223. Compared to this approach, our more complex model removes mass from the individual supercluster constituents and redistributes it to the filament component. Reproducing the two-component fit with free concentration parameters, which was used in the previous study, we find  $M_{200}(\text{A 222}) = (2.7^{+0.8}_{-0.7}) \times 10^{14} M_{\odot}$ , which is in good agreement, and  $M_{200}(\text{A 223}) = (3.4^{+1.3}_{-1.0}) \times 10^{14} M_{\odot}$ , which overlaps the  $1\sigma$  error bars of the earlier study. Here and in the following, all error bars are single standard deviations.

The detection of a filament with a dimensionless surface mass density of  $\kappa \sim 0.03$  is unexpected. Simulations generally predict the surface mass density of filaments to be much lower<sup>10</sup> and not to be detectable individually<sup>18</sup>. These predictions, however, are based on the assumption that the longer axis of the filament is aligned with the plane of the sky and that we look through

the filament along its minor axis. If the filament were inclined with respect to the line-of-sight and we were to look almost along its major axis, the projected mass could reach the observed level. A timing argument<sup>19,20</sup> can be made to show that the latter scenario is more plausible in the A 222/3 system. In this argument we treat A 223 as a single cluster and neglect the filament component, such that we have to deal only with two bodies, A 222 and A 223. The redshifts of A 222 and A 223 differ by  $\Delta z = 0.005$ , corresponding to a line-of-sight separation of 18 Mpc if the redshift difference is entirely due to Hubble flow. Let us assume for a moment that the difference is caused only by peculiar velocities. Then at  $z = \infty$ , the clusters were at the same location in the Hubble flow. We let them move away from each other with some velocity and inclination angle with respect to the line-of-sight and later turn around and approach each other. The parameter space of total system mass and inclination angle that reproduces the observed configuration at  $z = 0.21$  is completely degenerate. Nevertheless, in order to explain the observed configuration purely with peculiar velocity, this model requires a minimum mass of  $(2.61 \pm 0.05) \times 10^{15} M_{\odot}$  with an inclination angle of 46 degrees, where the error on the mass is caused solely by the uncertainty of the Hubble constant. Since this is more than 10 standard deviations above our mass estimate for the sum of both clusters, we infer that at least part of the observed redshift difference is due to Hubble flow, and that we are looking along the filament's major axis.

The combination of our weak-lensing detection with the observed X-ray emission of  $0.91 \pm 0.25$  keV WHIM plasma<sup>4</sup> lets us constrain the hot gas fraction in the filament. Assuming that the distribution of the hot plasma is uniform and adopting a metallicity of  $Z = 0.2$  Solar, the mass of the X-ray emitting gas inside a cylindrical region with radius 330 kpc centred on (01:37:45.00, 12:54:19.6, Figure 3) with a length along our line-of-sight of  $l = 18$  Mpc, as suggested by our timing argument, is  $M_{\text{gas}} = 5.8 \times 10^{12} M_{\odot}$ . The assumption of uniform density is certainly a strong simplification. Because the X-ray emissivity depends on the average of the squared gas density, a non-uniform density distribution can lead to strong changes in the X-ray luminosity. Thus, if the filament consists of denser clumps embedded into lower density gas (as has been observed in the outskirts of the Perseus Cluster<sup>21</sup>), or even if there is a smooth non-negligible density gradient within the region used for spectral extraction, then our best fit mean density will be overestimated. The quoted gas mass should therefore be considered as an upper limit, and the true mass may be lower by up to a factor of 2–3.

We estimated the total mass of the filament from the reconstructed surface mass-density map and the model fits within the same region where we measured the gas mass. The conversion of dimensionless surface mass density to physical units requires knowledge of the source redshifts. We randomly sampled galaxies with our  $R_c$ -band magnitude distribution from photometric redshift catalogues<sup>22</sup>. The mean redshift of these random catalogues is  $z_s = 1.2$ . We emphasize that for a cluster at  $z = 0.21$ , the error in mass caused by the uncertainty of the redshift distribution is small. An error as large as  $\Delta z_s = 0.2$  causes only a 5% error. In the reconstructed  $\kappa$ -map, the mass inside the extraction circle is  $M_{\text{fil}} = (6.5 \pm 0.1) \times 10^{13} M_{\odot}$ , where the error is small due to the highly correlated noise of the smoothed shear field inside the extraction aperture. For the parametric model fit, the inferred mass is higher but consistent within one standard deviation,

$M_{\text{fil}} = (9.8 \pm 4.4) \times 10^{13} M_{\odot}$ . The corresponding upper limits on the hot gas fractions vary between  $f_X = 0.06 - 0.09$ , a value that is lower than the gas fraction in galaxy clusters<sup>23</sup>. This is consistent with the expectation that a significant fraction of the WHIM in filaments is too cold to emit X-rays detectable by XMM-Newton<sup>24</sup>.

1. Bond, J. R., Kofman, L. & Pogosyan, D. How filaments Are Woven into The Cosmic Web. *Nature* **380**, 603–606 (1996).
2. Joeveer, M., Einasto, J. & Tago, E. Spatial distribution of galaxies and of clusters of galaxies in the southern galactic hemisphere. *Mon. Not. R. Astron. Soc.* **185**, 357–370 (1978).
3. Geller, M. J. & Huchra, J. P. Mapping the universe. *Science* **246**, 897–903 (1989).
4. Werner, N. *et al.* Detection of hot gas in the filament connecting the clusters of galaxies Abell 222 and Abell 223. *Astron. Astrophys.* **482**, L29–L33 (2008). 0803.2525.
5. Buote, D. A. *et al.* X-Ray Absorption by WHIM in the Sculptor Wall. *Astrophys. J.* **695**, 1351–1356 (2009). 0901.3802.
6. Fang, T. *et al.* Confirmation of X-ray Absorption by Warm-Hot Intergalactic Medium in the Sculptor Wall. *Astrophys. J.* **714**, 1715–1724 (2010). 1001.3692.
7. Aragón-Calvo, M. A., van de Weygaert, R. & Jones, B. J. T. Multiscale phenomenology of the cosmic web. *Mon. Not. R. Astron. Soc.* **408**, 2163–2187 (2010). 1007.0742.
8. Kaiser, N. *et al.* A Photometric and Weak Lensing Analysis of the  $z=0.42$  Supercluster MS0302+17. *astro-ph/9809268* (1998).
9. Gray, M. E. *et al.* Probing the Distribution of Dark Matter in the A901/902 Supercluster with Weak Lensing. *Astrophys. J.* **568**, 141–162 (2002).
10. Dietrich, J. P., Schneider, P., Clowe, D., Romano-Díaz, E. & Kerp, J. Weak lensing study of dark matter filaments and application to the binary cluster A 222 and A 223. *Astron. Astrophys.* **440**, 453–471 (2005).
11. Gavazzi, R., Mellier, Y., Fort, B., Cuillandre, J.-C. & Dantel-Fort, M. Mass and light in the supercluster of galaxies MS0302+17. *Astron. Astrophys.* **422**, 407–422 (2004).
12. Heymans, C. *et al.* The dark matter environment of the Abell 901/902 supercluster: a weak lensing analysis of the HST STAGES survey. *Mon. Not. R. Astron. Soc.* **385**, 1431–1442 (2008). 0801.1156.
13. Dietrich, J. P., Clowe, D. I. & Soucail, G. Spectroscopy of the neighboring massive clusters Abell 222 and Abell 223. *Astron. Astrophys.* **394**, 395–403 (2002).
14. Navarro, J. F., Frenk, C. S. & White, S. D. M. A Universal Density Profile from Hierarchical Clustering. *Astrophys. J.* **490**, 493–508 (1997).

15. Dolag, K. *et al.* Numerical study of halo concentrations in dark-energy cosmologies. *Astron. Astrophys.* **416**, 853–864 (2004). [arXiv:astro-ph/0309771](#).
16. King, I. R. The structure of star clusters. III. Some simple dynamical models. *Astron. J.* **71**, 64–75 (1966).
17. Colberg, J. M., Krughoff, K. S. & Connolly, A. J. Intercluster filaments in a  $\Lambda$ CDM Universe. *Mon. Not. R. Astron. Soc.* **359**, 272–282 (2005). [arXiv:astro-ph/0406665](#).
18. Mead, J. M. G., King, L. J. & McCarthy, I. G. Probing the cosmic web: intercluster filament detection using gravitational lensing. *Mon. Not. R. Astron. Soc.* **401**, 2257–2267 (2010). [0910.2417](#).
19. Kahn, F. D. & Woltjer, L. Intergalactic Matter and the Galaxy. *Astrophys. J.* **130**, 705–717 (1959).
20. Sandage, A. The redshift-distance relation. IX - Perturbation of the very nearby velocity field by the mass of the Local Group. *Astrophys. J.* **307**, 1–19 (1986).
21. Simionescu, A. *et al.* Baryons at the Edge of the X-ray-Brightest Galaxy Cluster. *Science* **331**, 1576– (2011). [1102.2429](#).
22. Ilbert, O. *et al.* Accurate photometric redshifts for the CFHT legacy survey calibrated using the VIMOS VLT deep survey. *Astron. Astrophys.* **457**, 841–856 (2006). [arXiv:astro-ph/0603217](#).
23. Allen, S. W. *et al.* Improved constraints on dark energy from Chandra X-ray observations of the largest relaxed galaxy clusters. *Mon. Not. R. Astron. Soc.* **383**, 879–896 (2008). [0706.0033](#).
24. Davé, R. *et al.* Baryons in the Warm-Hot Intergalactic Medium. *Astrophys. J.* **552**, 473–483 (2001). [arXiv:astro-ph/0007217](#).
25. Miller, L., Kitching, T. D., Heymans, C., Heavens, A. F. & van Waerbeke, L. Bayesian galaxy shape measurement for weak lensing surveys - I. Methodology and a fast-fitting algorithm. *Mon. Not. R. Astron. Soc.* **382**, 315–324 (2007). [arXiv:0708.2340](#).
26. Kitching, T. D., Miller, L., Heymans, C. E., van Waerbeke, L. & Heavens, A. F. Bayesian galaxy shape measurement for weak lensing surveys - II. Application to simulations. *Mon. Not. R. Astron. Soc.* **390**, 149–167 (2008). [0802.1528](#).

**Supplementary Information** is linked to the online version of the paper at [www.nature.com/nature](http://www.nature.com/nature)

**Acknowledgements** JPD was supported by NSF grant AST 0807304. AS acknowledges support from the National Aeronautics and Space Administration through the Einstein Postdoctoral Fellowship Award Number PF9-00070.

**Author Contributions** JPD led the project, reduced the optical data, performed the weak lensing analysis and wrote the manuscript. NW contributed to the writing of the manuscript. NW, AF, and AS performed the X-ray analysis and estimated the gas mass. The timing argument was made by DC. LM and TK wrote the shear estimation code. All authors discussed all results and commented on the manuscript.

**Competing Interests** The authors declare that they have no competing financial interests.

**Correspondence** Correspondence and requests for materials should be addressed to JPD (email: jorgd@umich.edu).



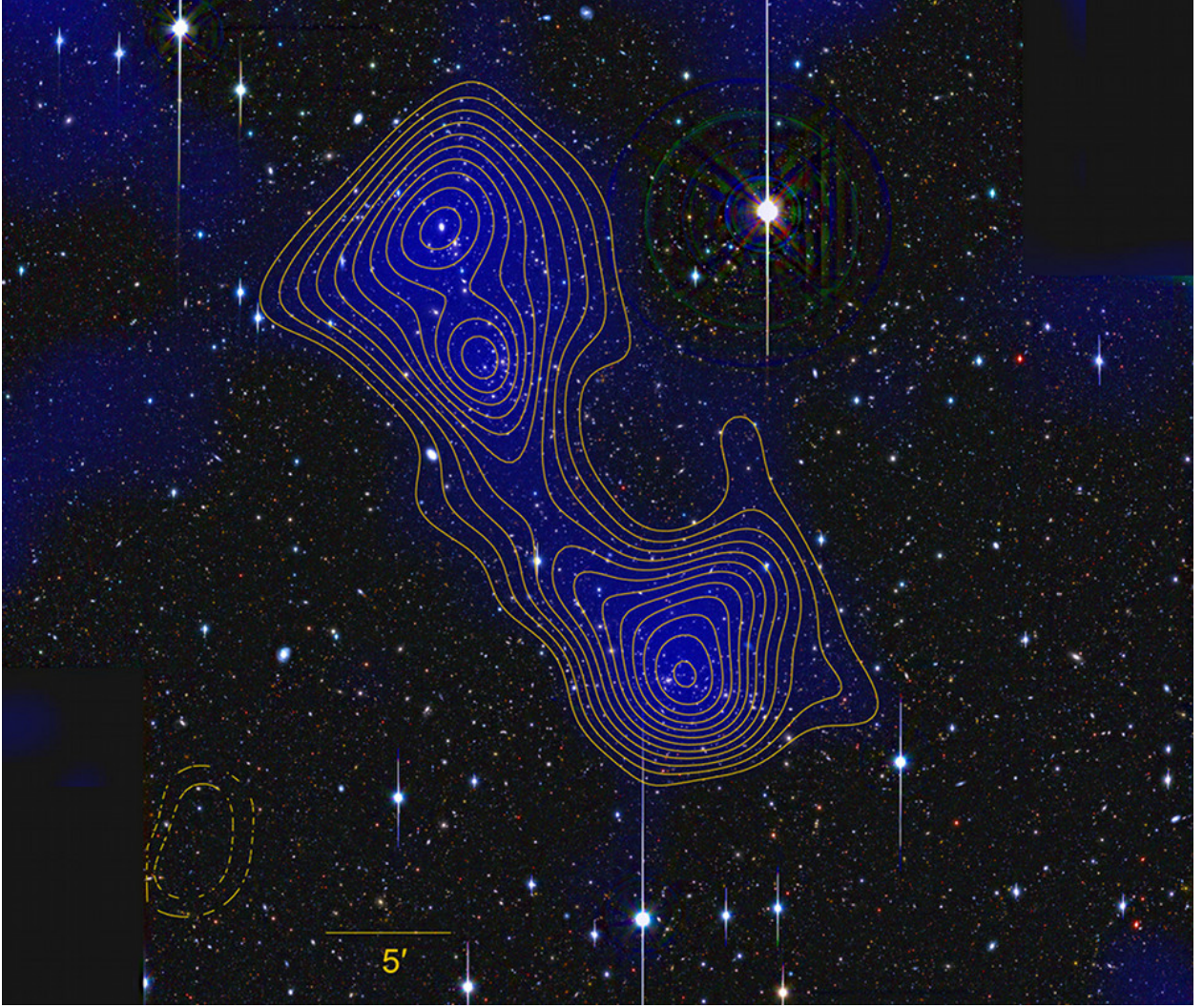


**Figure 1: Mass reconstruction of A 222/223.** The background image is a three colour-composite SuprimeCam image based on observations with the 8m Subaru telescope during the nights of Oct. 15 (A 222) and 20 (A 223), 2001 in V-,  $R_c$ - and  $i'$ -bands. We obtained the data from the SMOKA science archive (<http://smoka.nao.ac.jp/>). The FWHM of the stellar point-spread function varies between  $0''.57$  and  $0''.70$  in our final co-added images. Overlaid are the reconstructed surface mass density (blue) above  $\kappa = 0.0077$ , corresponding to  $\Sigma = 2.36 \times 10^{13} M_\odot \text{Mpc}^{-2}$ , and significance contours above the mean of the field edge, rising in steps of  $0.5\sigma$  and starting from  $2.5\sigma$ . Dashed contours mark underdense regions at the same significance levels. Supplementary Figure 1 shows the corresponding B-mode map. The reconstruction is based on 40,341 galaxies whose colours are not consistent with early type galaxies at the cluster redshift. The shear field was smoothed with a  $2'$  Gaussian. The significance was assessed from the variance of 800 mass maps created from catalogues with randomised background galaxy orientation. We measured the shapes of these galaxies primarily in the  $R_c$ -band, supplementing the galaxy shape catalogue with measurements from the other two bands for galaxies for which no shapes could be measured in the  $R_c$ -band, to estimate the gravitational shear<sup>25,26</sup>. A 222 is detected at  $\sim 8.0\sigma$  in the south, A 223 is the double-peaked structure in the north seen at  $\sim 7\sigma$ .

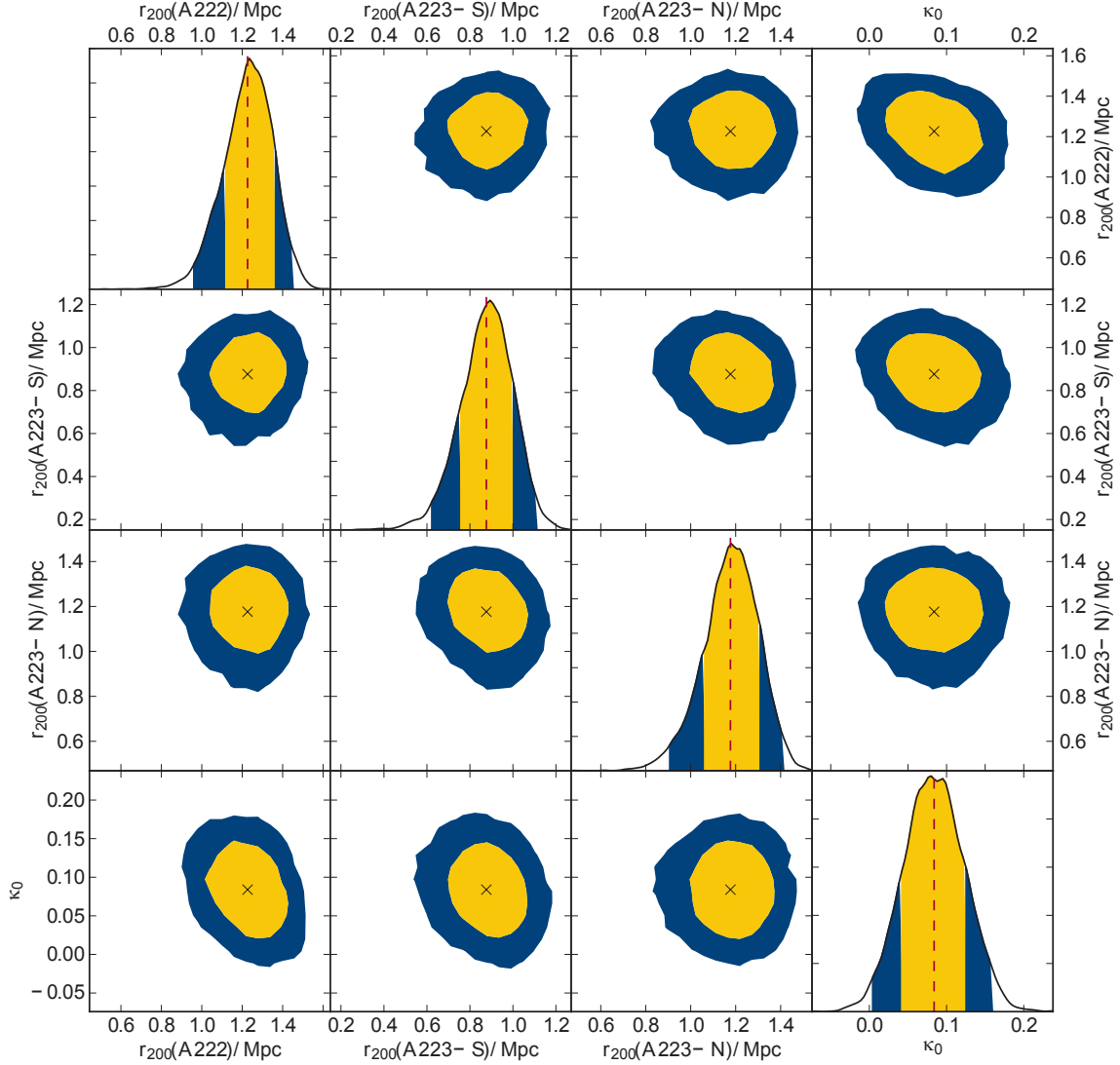


**Figure 2: Posterior probability distributions for cluster virial radii and filament strength.** Shown are the 68% and 95% confidence intervals on the cluster virial radii  $r_{200}(\cdot)$  and the filament strength  $\kappa_0$ . The confidence intervals are derived from 30,000 MCMC sample points. The filament model is described by  $\kappa(\theta, r) = \kappa_0 \left\{ 1 + \exp \left[ \frac{(|\theta| - \theta_1)}{\sigma} \right] + \left( \frac{r}{r_c} \right)^2 \right\}^{-1}$ , where the coordinate  $\theta$  runs along the filament ridge line and  $r$  is orthogonal to it. This model predicts the surface mass density at discrete grid points from which we computed our observable, the reduced shear, via a convolution in Fourier space. The data cannot constrain the steepness of the exponential cut-off at the filament endpoints  $\sigma$  and the radial core scale  $r_c$ . These were fixed at their approximate best-fit values of  $\sigma = 0.45$  Mpc and  $r_c = 0.54$  Mpc. The data also cannot constrain the cluster ellipticity and orientation. These were held fixed at the values measured from the isodensity contours of early-type galaxies<sup>13</sup>. The ratios of minor/major axes and the position angles of the ellipses are (0.63, 0.69, 0.70) and (65°, 34°, 3°) for A 222, A 223-S, and A 223-N, respectively. We further explore the impact of cluster ellipticity on the filament detection in the supplementary information.



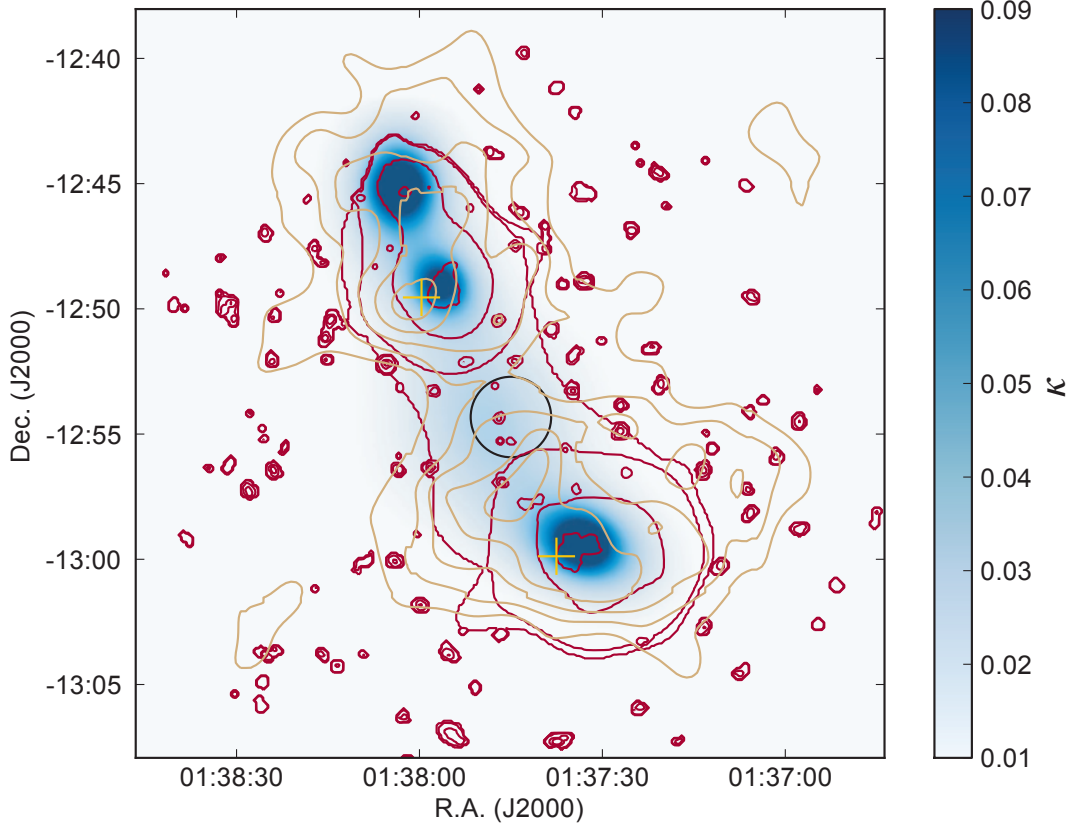


**Figure 3: Surface mass density of the best fit parametric model.** The surface mass density distribution of the best parameters in Fig. 2 was smoothed with a  $2'$  Gaussian to have the same physical resolution as the mass reconstruction in Fig. 1. The yellow crosses mark the end points of the filament model. These were determined from the visual impression of the filament axis in Fig. 1. The MCMC is not able to constrain their location. In the model, the filament ridge line is not aligned with the axis connecting the centers of A 222 and A 223-S. This is a fairly common occurrence ( $\sim 9\%$ ) for straight filament but may also indicate some curvature, which occurs in  $\sim 53\%$  of all intercluster filaments<sup>17</sup> and is not included in our simple model. Overlaid are X-ray contours from XMM-Newton observations<sup>4</sup> (red) and significance contours of the colour-selected early-type galaxy density<sup>10</sup> (beige), showing the alignment of all three filament constituents. The black circle marks the region inside which the gas mass and the filament mass were estimated.

## Supplementary Information

In this document we provide additional information on the data reduction, shear measurement, and tests performed.

### S1 Data

We reduced the data using the publicly available THELI pipeline<sup>27</sup>. The data were astrometrically calibrated against the USNO-B1.0 catalogue, which has a precision of  $\sim 0''.2$ . Since this is insufficient to align objects on dithered exposure without introducing errors in the gravitational shear measurement, THELI uses the SWARP calibration software to align images internally. The astrometric residuals in this process are smaller than  $0''.02$  or a tenth of a pixel.

No photometric standards were observed in the nights our data was taken. We calibrated our  $R_c$ -band data against the catalogue of our earlier study of this system<sup>10</sup>. We fixed the zero-points of the other two bands by matching the expected colours of stars from the Pickles stellar library<sup>28</sup> to the observed colours of stars in the field.

The gravitational shear was estimated independently in all three passbands using the lensfit algorithm<sup>25,26</sup>. Lensfit is a Bayesian model fitting code, which fits the sum of an exponential and a de Vaucouleurs profile to galaxies. The model fit has six free parameters, the galaxy position  $(x, y)$ , its ellipticity  $(e_1, e_2)$ , brightness, bulge-fraction, and galaxy scale  $r$ . The model fitting is done in Fourier space so that the brightness and position can be marginalised over analytically. The radius and bulge-fraction are marginalised over numerically, leaving a likelihood surface as a function of  $(e_1, e_2)$ . Lensfit acts on the individual exposures and generates a posterior probability for each galaxy by summing over the posterior ellipticity distributions generated by measurements in each exposure.

Because lensfit is a forward fitting method, its model space needs to be convolved with a PSF model describing the stellar point spread function at the location of each galaxy. We modelled the spatial variation of the PSF across the focal plane with a bivariate polynomial, whose zeroth and first order coefficients were allowed to vary from chip to chip.

Galaxy shapes are highly correlated across different passbands and simply combining shear estimates from different passbands entails the risk of degrading them to the band with the worst seeing or the largest remaining systematics. To maximise the lensing information from all three passbands we therefore chose a different route. We used shape measurements from the  $R_c$ -band data, which has the best seeing and is the deepest. For galaxies without  $R_c$ -band shape information, we used  $i'$ -band measurements, and in turn V-band measurements were used for galaxies that also have no  $i'$ -band shapes.

We used an empirical approach to find an optimal balance between the rejection of cluster/foreground galaxies and the density of our lensing catalogue. We placed aperture mass filters<sup>29</sup> on the three known structures in the field (A 222, A 223-S, A 223-N). For galaxies with two colours measured, we rejected galaxies inside a parallelogram placed on a colour-colour diagram. An MCMC algorithm moved the vertexes of this parallelogram to maximise the aperture mass signal. A similar procedure was used for galaxies with one colour measured, either  $V - R_c$  or  $R_c - i'$ . A rectangle inside which galaxies were rejected from the lensing catalogue was placed on a colour-magnitude diagram. Again, the corners of this rectangle were moved to maximise the aperture mass signal. For both procedures, a maximum magnitude, down to which the colour cut was applied, was determined at the same time. Finally, for galaxies observed in only one passband, we imposed a magnitude cut in the same way.

This method rejected galaxies with colours consistent with early-type galaxies at the cluster redshift and showed that fainter galaxies produce a stronger aperture mass signal than brighter ones. Both properties are indications that we measure a real cluster signal and that the redshift scaling of the lensing signal is at least approximately correct. At the same time we find that colour and magnitude cuts made to maximise the aperture mass signal of the known clusters, also lead to an increase in the lensing strength of the filament. This supports our view that the filament is a real structure located at the same redshift as the galaxy clusters.

We also note that the filament is seen in mass reconstructions generated from lensing catalogues of the individual passbands, but at lower levels consistent with the shallower data. In the  $R_c$ -band reconstruction, a mass bridge is present at the  $3.5\sigma$  level. In the V- and  $i'$ -band it is seen at the  $2\sigma$  and  $2.5\sigma$  level, respectively. We emphasise again that one cannot simply combine these significances in quadrature because a large covariance exists between the shear estimates in different passbands.

Finally, we show E- and B-mode reconstructions of our combined lensing catalogue to test for PSF modelling systematics (Figure S1).

## S2 Fitting elliptical profiles

The ellipticity of the clusters connected by a filament has the potential to be confused with the filament itself and may in extreme cases even lead to the visual impression of a filament even if the clusters' mass distribution is completely described by elliptical NFW halos. In this section we further explore the influence of cluster ellipticity on the significance of our filament detection.

To recapitulate, we modelled the clusters with fixed ellipticities measured from the distribution of their early type galaxies. In this configuration, A 223-S points almost exactly along the filament ridgeline and A 222 is about halfway turned towards the filament. Consequentially both clusters contribute more mass towards the filament area than they would in a spherical configu-

ration. This is reflected in small differences in the filament significance if we fit three spherical clusters. In this case, the integrated mass along the filament exceeds that of the three clusters only case in 98.9% compared to 98.5% for the fixed ellipticities. The likelihood-ratio test prefers three spherical clusters plus a filament over a model with only three spherical clusters at 97.8% confidence, compared to the 96.0% significance for the fixed ellipticities used in the main paper. The filament mass in the case of spherical halos is higher by about 30%. This is within the error bars we report but easily explained by the diminished contribution of A 222 and A 223-S to the surface mass density in the filament region.

We used fixed cluster ellipticities because the data is not able to constrain the ellipticity, as evidenced by Figure S2. However, even though we allowed for more elongated halo shapes and for A 222 to point exactly along the filament ridgeline, the marginalised probability distribution of  $\kappa_0$  shows that a positive filament distribution is still strongly favoured. Again the integrated surface mass density along the filament exceeds that of a model without filament component for 98.4% of all sample points and the likelihood ratio test prefers the presence of a filament at 98.2% significance. The latter number is noticeably higher than what we report for fixed cluster ellipticities. The reason is that the “best fit” values, which are really unconstrained, have A 223-S oriented perpendicular to the filament. As a result, the presence of a filament is even more strongly required than in the configuration we considered in the main body of the paper. The likelihood-ratio test shows that elliptical clusters are slightly preferred by the data over spherical ones (84.3%), but – as suggested by the flat posteriors on  $q$  – no preference exists for the specific values of axis ratios and position angles chosen by us (19.5%). In light of what the data tell us, we thus consider our choice of cluster ellipticities to be conservative.

27. Erben, T. *et al.* GaBoDS: The Garching-Bonn Deep Survey. IV. Methods for the image reduction of multi-chip cameras demonstrated on data from the ESO Wide-Field Imager. *Astronomische Nachrichten* **326**, 432–464 (2005).
28. Pickles, A. J. A Stellar Spectral Flux Library: 1150–25000 Å. *PASP* **110**, 863–878 (1998).
29. Schneider, P. Detection of (dark) matter concentrations via weak gravitational lensing. *Mon. Not. R. Astron. Soc.* **283**, 837–853 (1996).
30. van Waerbeke, L. Noise properties of gravitational lens mass reconstruction. *Mon. Not. R. Astron. Soc.* **313**, 524–532 (2000).
31. Kasun, S. F. & Evrard, A. E. Shapes and Alignments of Galaxy Cluster Halos. *Astrophys. J.* **629**, 781–790 (2005).

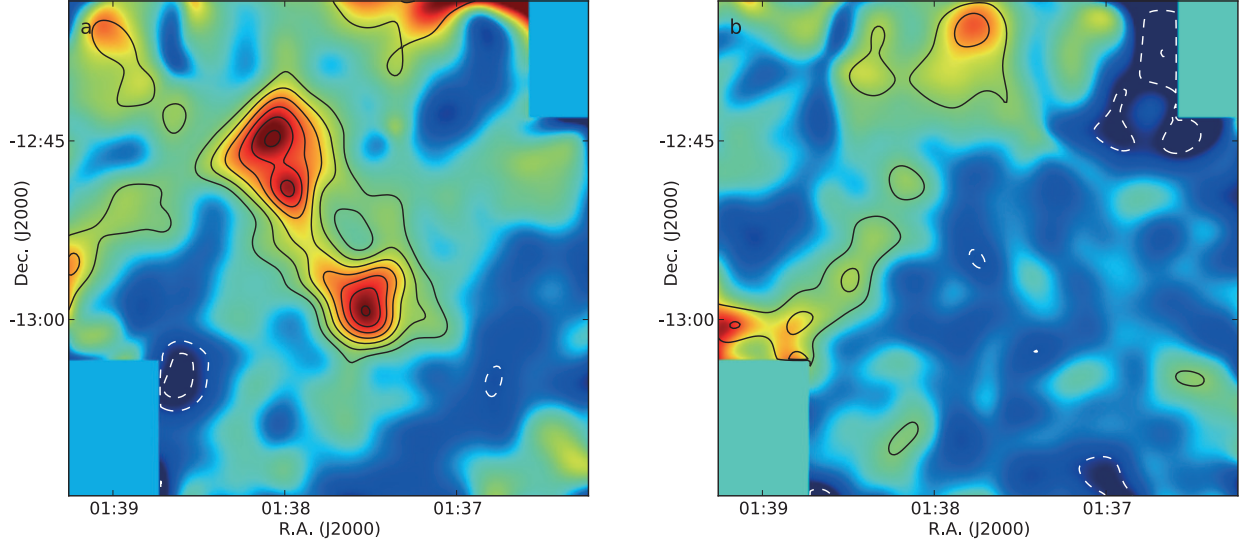


**Figure S1: E- and B-mode reconstructions.** Panel a again shows the mass reconstruction from Figure 1. The colour scale in the background is dimensionless surface mass density and the contours are significance contours starting at  $2\sigma$  and rising in steps of  $1\sigma$  above the mean of the field edges (solid black), excluding the top edge, which is strongly affected by stray-light. Dashed white contours are at the same negative levels. Panel b shows a mass reconstruction of the B-modes, obtained by rotating all galaxies by  $45^\circ$ . More and/or higher peaks than expected from a Gaussian random field would be an indicator of systematic residuals in the shear estimation. The peak count here is consistent with expectations for a pure noise field<sup>30</sup>. The shear field in both panels was smoothed with a  $2'$  Gaussian. Both panels have identical colour scales.

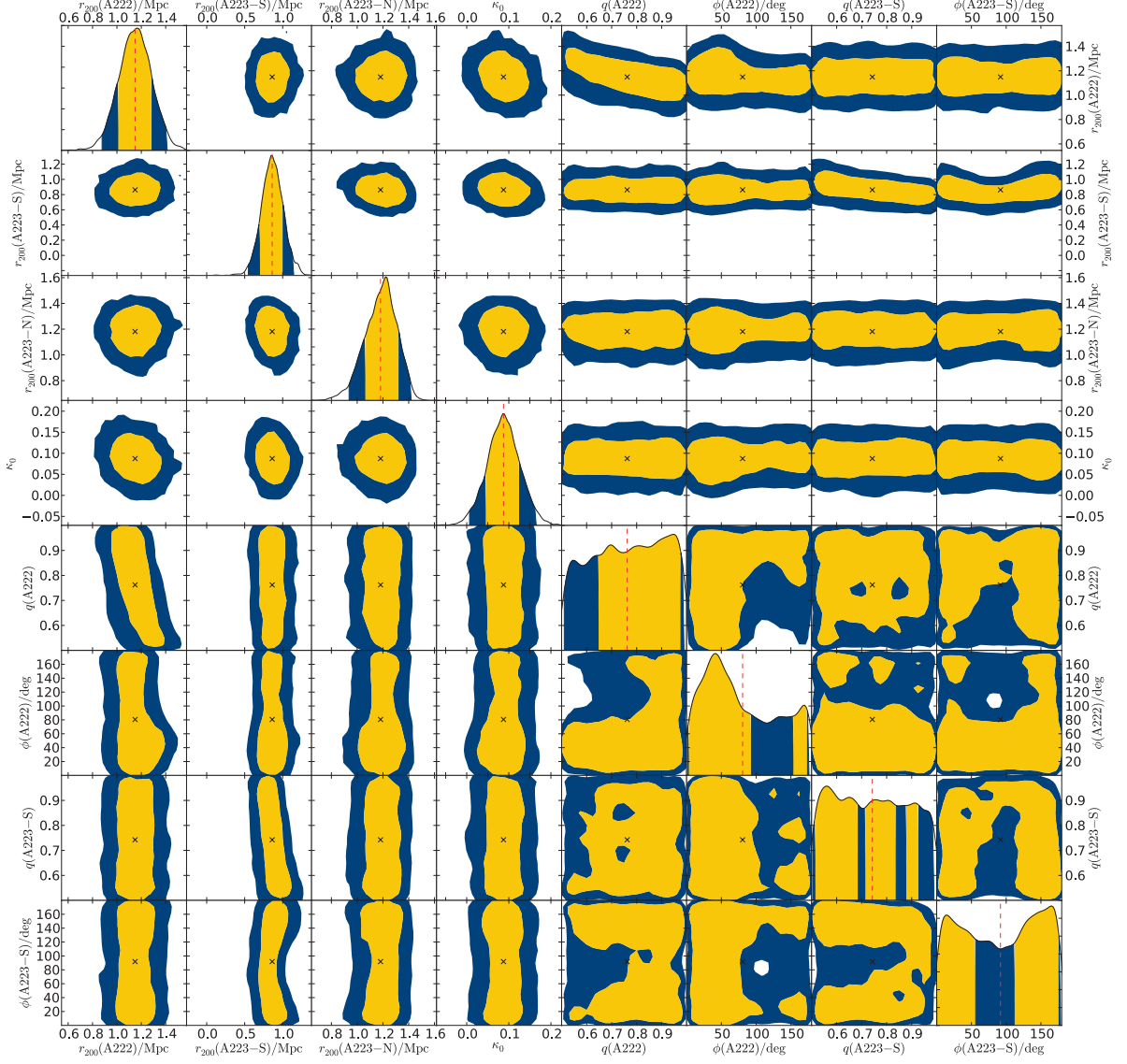


**Figure S2: Posterior probability distributions with free ellipticities.** Similar to Figure 2 we show the 68% and 95% confidence contours on the cluster virial radii  $r_{200}(\cdot)$  and filament strength  $\kappa_0$ . In addition we tried to constrain the cluster axis ratios  $q(\cdot)$  and position angles  $\phi(\cdot)$  for A 222 and A 223-S. Their values for A 223-N were held fixed at those used in the main paper, as the mass distribution of A 223-N shows no degeneracy with the filament strength. We put a flat prior  $0.5 < q < 1$  on the axis ratio to encompass all but the most elliptical halos<sup>31</sup>. This also includes the values used in the main paper. Allowing for more extreme axis ratios does not seem to be warranted by the absence of a trend in the filament strength with axis ratios.